International Journal of Fatigue 164 (2022) 107121

Contents lists available at ScienceDirect

International Journal of Fatigue

journal homepage: www.elsevier.com/locate/ijfatigue

On the use of the cumulative strain energy density for fatigue life assessment in advanced high-strength steels

R. Branco [a], R.F. Martins [b], J.A.F.O. Correia [c], Z. Marciniak [d], W. Macek [e], J. Jesus [f,a]

[a] CEMMPRE, Department of Mechanical Engineering, University of Coimbra, Rua Luís Reis Santos, Coimbra, 3030-788 Coimbra, Portugal
[b] UNIDEMI, Department of Mechanical and Industrial Engineering, Nova School of Science and Technology, Universidade NOVA de Lisboa, Campus de Caparica, 2829-516 Caparica, Portugal
[c] INEGI & CONSTRUCT, Faculty of Engineering, University of Porto, Rua Dr. Roberto Frias, 4200-465 Porto, Portugal
[d] Opole University of Technology, Faculty of Mechanical Engineering, 45-271 Opole, Mikolajczyka 5, Poland
[e] Faculty of Mechanical Engineering and Ship Technology, Gdańsk University of Technology, 11/12 Gabriela Narutowicza Street, 80-233 Gdańsk, Poland
[f] Department of Mechanical Engineering, Lisbon Polytechnic – ISEL, Rua Conselheiro Emídio Navarro 1, 1959-007 Lisboa, Portugal

ARTICLE INFO

Keywords:
Cumulative strain energy density
Low-cycle fatigue
High-strength steels
Fatigue life prediction
Fatigue indicator parameter

ABSTRACT

In this paper, the applicability of the cumulative strain energy density is explored as a fatigue indicator parameter for advanced high-strength steels subjected to strain-controlled conditions. Firstly, the cyclic stress–strain responses of nine steels, selected from three multiphase families, encompassing different elemental compositions and different heat treatment routes, were studied. Then, the predictive capabilities of the proposed model were compared with those of other strain-based and energy-based approaches. It was found that the cumulative strain energy density decreases as the strain amplitude increaes. It was also found that the cumulative strain energy density and the fatigue life can be related via a power function. In addition, the relationship between the cumulative strain energy and the fatigue life was not significantly affected by the elemental composition or the heat treatment route. Finally, the fatigue lives computed through the cumulative strain energy density concept were close to those of the other models but were slightly more conservative.

1. Introduction

Advanced high-strength steels with multiphase microstructures are pivotal materials in modern engineering [1,2]. This new generation of steels has attracted considerable attention over the last decades because multiphase microstructures can maximise the benefits of each phase while reducing or eliminating the shortcomings of a particular phase by the presence of other phases [3,4]. The alloy design of these sophisticated materials is generally accomplished by optimisation of chemical compositions and by the definition of the most suitable routes of the multi-step heat treatments [2,5]. This makes the process laborious because the final mechanical properties are directly connected to the defined variables leading to complex problems.

Their superior mechanical properties make them particularly attractive for different strategic industries, such as automotive, railway, aerospace, shipbuilding, and infrastructure, among others. In these specific sectors, mechanical components are often subjected to dynamic loads due to their service nature, which may lead to damage accumulation at critical points. This damage accumulation, if not properly accounted for, can culminate in fatigue failure [6–10]. Thus, an efficient design against fatigue requires not only deep knowledge about the cyclic deformation behaviour but also the identification of adequate fatigue damage parameters capable of correlating the loading level with the fatigue lifetime [11–14].

The relationship between loading level and fatigue lifetime is generally defined using stress-based, strain-based, or energy-based approaches. Stress-based approaches are recommended for the high-cycle fatigue regime when cyclic plasticity is involved in localised regions. Strain-based approaches can be used most effectively in the low-cycle fatigue regime where significant plastic deformation exists. Finally, energy-based approaches, because they are defined through stress and strain variables, can deal with both low-cycle and high-cycle fatigue problems, which make them more attractive [15–19]. Due to this fact, this last group has received much attention and has inspired a number of alternative formulations [20–24].

As far as the alternative energy-based formulations are concerned, they are often based on the concept of the strain energy density of a single cycle, generally the half-life cycle. However, this snapshot, which

E-mail address: ricardo.branco@dem.uc.pt (R. Branco).

https://doi.org/10.1016/j.ijfatigue.2022.107121
Received 6 June 2022; Received in revised form 25 June 2022; Accepted 3 July 2022
Available online 13 July 2022

Table 1
Chemical composition of the tested steels (wt.%).

Material	C	Si	Mn	Cr	Ni	Mo	Al	Fe
Steel 1	0.27	1.7	0	1.9	0.4	0.4	0.6	Bal.
Steel 2	0.27	1.7	2.3	1.9	0.4	0.4	0.6	Bal.
Steel 3	0.27	1.7	3.2	1.9	0.4	0.4	0.6	Bal.
Steel 4	0.21	1.8	1.1	0.7	0.14	0.19	–	Bal.
Steel 5	0.21	1.8	1.1	0.7	0.14	0.19	–	Bal.
Steel 6	0.21	1.8	1.1	0.7	0.14	0.19	–	Bal.
Steel 7	0.18	1.7	2.9	0.8	–	0.26	–	Bal.
Steel 8	0.18	1.7	2.9	0.8	–	0.26	–	Bal.
Steel 9	0.18	1.7	2.9	0.8	–	0.26	–	Bal.

is assumed to be representative of the saturated state of the material, makes it more difficult to account for the typical transient cyclic stress–strain phenomena that take place in metallic materials under strain-control mode and that are likely to cause significant energy variations in critical points even for constant-amplitude loading [25,26]. Thus, the cumulative strain energy density concept, which can be related to the total absorbed energy to failure, can inherently assess the energy changes caused by time-varying loads, which is an interesting outcome.

Despite its high potential, very few studies have evaluated the fatigue performance of engineering materials under strain-controlled conditions using the cumulative strain energy density concept [27–30]. Halford [27] analysed a number of ferrous and non-ferrous metals and demonstrated that the cumulative strain energy density is a decreasing function of the strain amplitude and can be related to the fatigue life via a power function. Li et al. [28] examined the influence of tempering temperature on high-strength spring steel and concluded that the higher the tempering temperature, the lower the fatigue damage rate. Long et al. [29] found that the Mn content has no significant effect on cumulative strain energy density in bainitic rail steels.

Regarding the degree of accuracy of the cumulative strain energy density concept for low-cycle fatigue life prediction, limited work was done [31–35]. Shi et al. [31] evaluated the predictive capabilities of various energy-based models in high-performance structural steels and proved that cumulative-based parameters can provide reliable results. Martins et al. [32] and Sarkar et al. [33] also advocated that the cumulative strain energy density is a reliable alternative to other classical strain-life and energy-life models for the estimation of fatigue durability in rail steels. Callaghan et al. [34] used this energy-based quantifier to

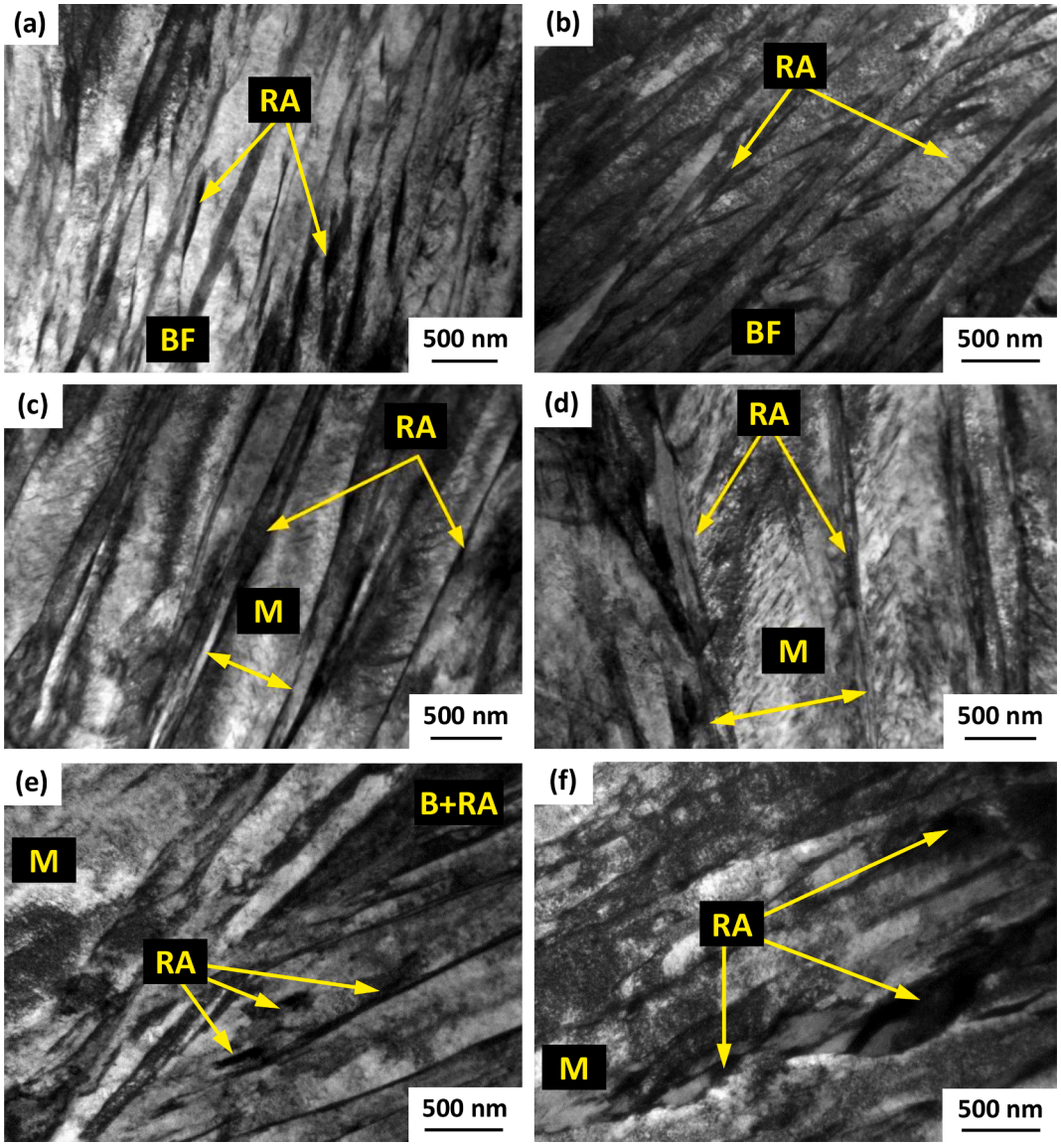

Fig. 1. TEM micrograph images of the tested steels: (a) bainitic steel (Steel 2); (b) bainitic steel (Steel 3); (c) martensitic steel (Steel 5); (d) martensitic steel (Steel 6); (e) low-carbon steel (Steel 7); (f) low-carbon steel (Steel 9). BF: Bainitic Ferrite; M: Martensite; RA: Retained Austenite.

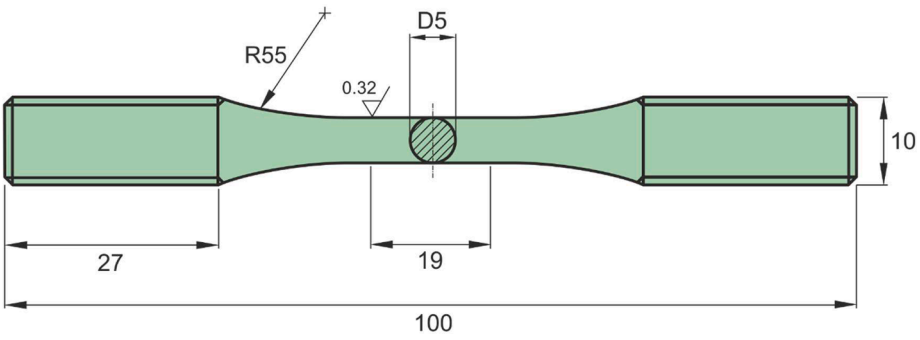

Fig. 2. Specimen geometry used in low-cycle fatigue tests (units: millimetres). Mean surface roughness in micrometres.

Table 2
Loading cases considered in the low-cycle fatigue tests.

Material	Strain amplitude, ε_a (%)	Reversals to failure, $2N_f$ (reversals)
Steel 1	0.60	8210
	0.70	4212
	0.80	3634
	1.00	1658
Steel 2	0.60	10,340
	0.70	6258
	0.80	2864
	1.00	968
Steel 3	0.60	26,740
	0.70	9066
	0.80	3792
	1.00	968
Steel 4	0.52	35,222
	0.60	5996
	0.70	3248
	0.80	4404
	1.00	2374
Steel 5	0.52	37,536
	0.60	17,180
	0.70	6244
	0.80	1378
	1.00	642
Steel 6	0.52	37,536
	0.60	17,180
	0.70	6244
	0.80	1378
	1.00	642
Steel 7	0.50	37,812
	0.65	7020
	0.80	2746
	1.00	1474
Steel 8	0.50	12,083
	0.65	3294
	0.80	1595
	1.00	801
Steel 9	0.50	9261
	0.65	2452
	0.80	925
	1.00	588

compute the fatigue life to crack propagation in ferritic steel at elevated temperature. More recently, Branco et al. [35] used the cumulative strain energy density to predict the crack initiation life in martensitic steels under multiaxial loading.

In sum, systematic studies dealing with advanced high-strength steels are scarce in the open literature. Thus, this paper aims to explore the use of the cumulative strain energy density to assess the fatigue life in advanced high-strength steels subjected to strain-controlled conditions. First, nine different steels selected from three multiphase families with different elemental compositions and heat treatment routes were studied. Then, the predictive capabilities of the proposed model based on the cumulative strain energy density concept were compared with those of other strain-based and energy-based models.

2. Materials and experiments

The materials selected for this study included various advanced high-strength steels, selected from three multiphase families, namely bainitic steels, martensitic steels, and low-carbon steels. This wide range of materials aimed at studying the influence on cumulative strain energy density of different elemental contents and tempering temperatures. Table 1 summarises the chemical composition, in weight percentage, of the different high-strength steels utilised in this research.

Regarding the heat treatment routes, these alloys were elaborated as follows:

- The first group, Steel 1 to Steel 3, which comprised three bainitic steels with different Mn contents, was austenitised at 930 °C for 45 min and then cooled from $M_S + 10$ °C to $M_S - 20$ °C to produce a bainitic microstructure (martensite start transformation, M_s, was equal to 390 °C, 370 °C, and 290 °C, respectively);
- The second group, Steel 4 to Steel 6, which covered a martensitic steel tempered at three different temperatures, was austenitised at 900 °C for 10 min, followed by tempering (at 320 °C, 350 °C, and 380 °C, respectively) for 1 h, and then was cooled to room temperature in air;
- The third group, Steel 7 to Steel 9, which included a low-carbon multiphase steel tempered at three different temperatures, was austenitised at 900 °C for 10 min, followed by tempering (at 230 °C, 275 °C, and 315 °C, respectively) for 2 h, and then quenched to room temperature at 25 °C.

More detailed information about the alloy design process of these advanced high-strength steels can be found in the articles [5,36,37].

Fig. 1 shows the typical microstructures obtained by transmission electron microscopy (TEM) for the three selected multiphase families [5,36,37]. Based on the TEM analysis, we can conclude that:

- The bainitic steel with the lowest content of Mn, Steel 1, was mainly formed by blocky ferrite and small amounts of bainitic ferrite plates, while the other two, Steel 2 and Steel 3, which had higher Mn contents, exhibited bainitic ferrite plates and film-like retained austenite (see Fig. 1(a) and Fig. 1(b));

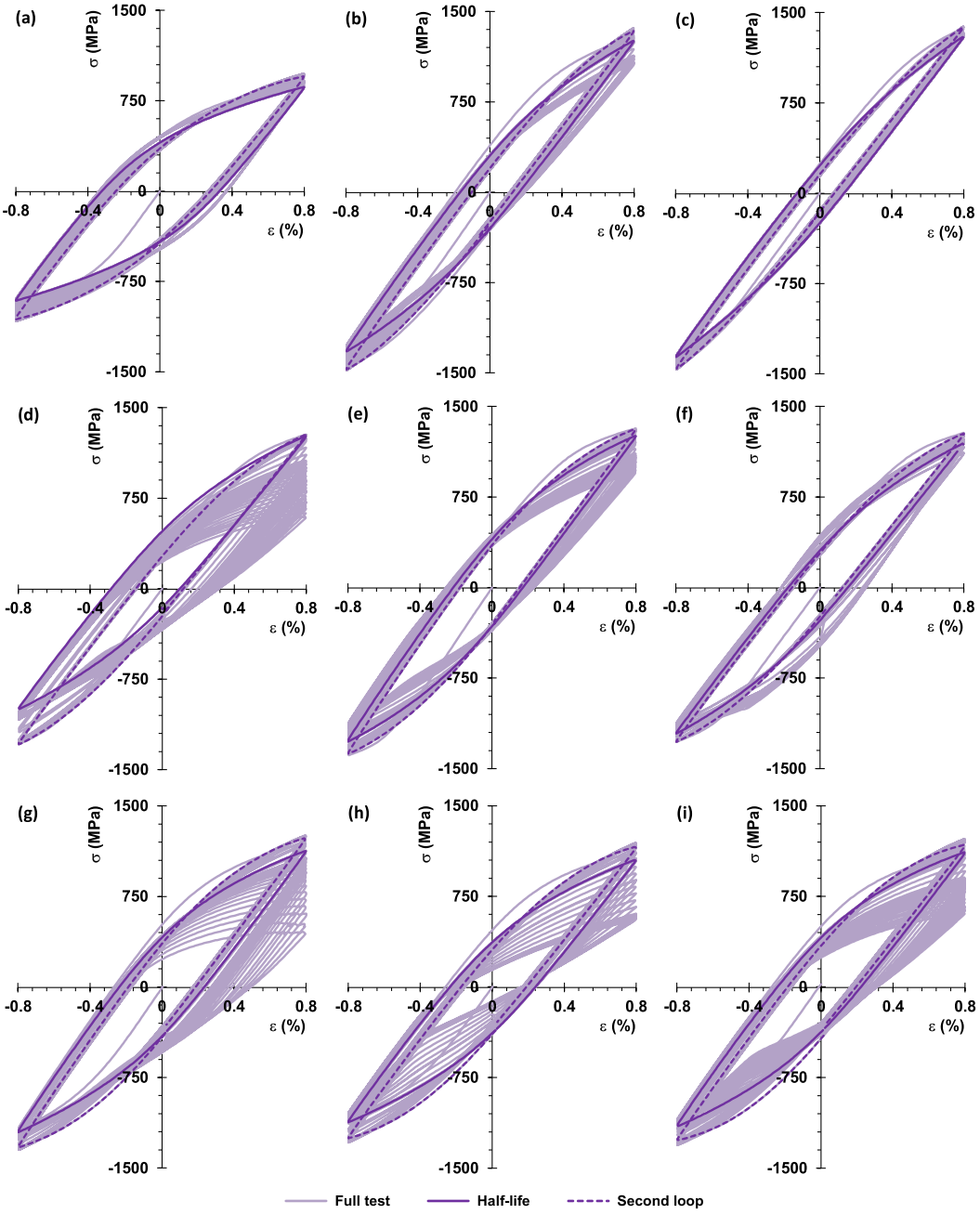

Fig. 3. Cyclic stress–strain response under strain-controlled conditions of the tested steels for the same strain amplitude ($\varepsilon_a = 0.8\%$): (a) Steel 1; (b) Steel 2; (c) Steel 3; (d) Steel 4; (e) Steel 5; (f) Steel 6; (g) Steel 7; (h) Steel 8; (i) Steel 9.

- The microstructure of the martensitic steels, Steel 4 to Steel 6, was relatively dense and contained laths of martensite along with residual austenite films. The width of the laths was small and there were high-density dislocations inside the laths. The increase of the tempered temperature resulted in both wider martensite laths and smaller dislocation densities (see Fig. 1(c) and Fig. 1(d));
- The low-carbon steel, Steel 7 to Steel 9, was mainly composed of a multiphase microstructure formed by bainite and martensite. The increase of the austempering temperature led to a higher number of blocky retained austenite and also to thicker and coarser body-centred cubic transformation products (see Fig. 1(e) and Fig. 1(f)).

A more comprehensive description of the microstructure features of the tested alloys can be found in the articles [5,36,37].

The low-cycle fatigue tests were run under strain-controlled conditions at a strain ratio (R_ε) of −1 and a strain rate ($d\varepsilon/dt$) of $6 \times 10^{-3}\ s^{-1}$ for strain amplitudes (ε_a) in the range 0.52%–1.0%. The cyclic stress–strain response was recorded using a 10 mm-long mechanical extensometer connected directly to the gauge section of the specimen. The

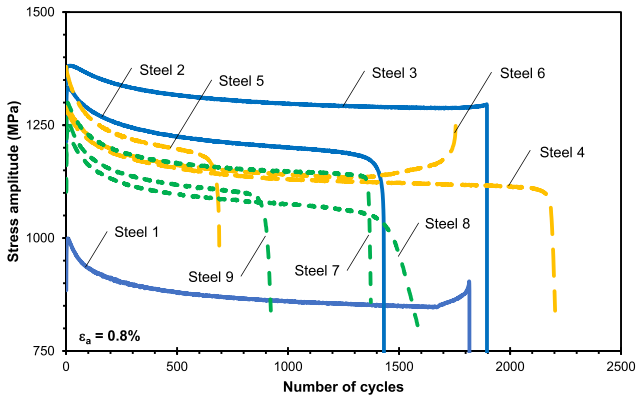

Fig. 4. Stress amplitude versus number of cycles at a fixed strain amplitude (ε_a = 0.8%) for the tested steels.

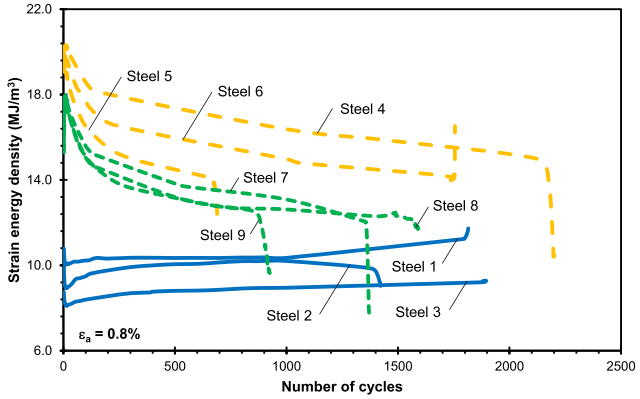

Fig. 5. Strain energy density versus number of cycles at a fixed strain amplitude (ε_a = 0.8%) for the tested steels (strain energy density calculated as the sum of both the plastic and the positive elastic components).

specimen geometry is schematised in Fig. 2. The tests started in compression and stopped when the specimen reached the total failure, or the maximum tensile stress decreased 25% relative to the initial value. Table 2 summarises the loading scenarios and the fatigue lives for the different steels.

3. Results and discussion

This section is divided into three subsections. Firstly, the cyclic stress–strain response of the tested steels is briefly addressed. Then, the strain-life relationships and the cumulative strain energy density versus life relationships are obtained. Finally, the predictive capabilities of the proposed model based on the cumulative strain energy density are compared with those of other classical strain-based and energy-based approaches.

3.1. Cyclic stress–strain response

Fig. 3 plots, as an example, the low-cycle fatigue behaviour at a fixed strain amplitude ($\varepsilon_a = \pm 0.8\%$) for various steels tested in this study. For the sake of comparability, the second loop (dashed lines) and the half-life loop (full line) are highlighted. Although the strain amplitude is fixed, the cyclic response, under strain-controlled conditions, is notoriously different, not only for the various families of advanced high-strength steels, but also for the same family produced with different features. Overall, we can see that these steels at this strain amplitude exhibit a strain-softening behaviour, i.e. the uncontrolled stress amplitude decreases gradually during the test up to the total failure.

The transient variations of the cyclic stress–strain response are generally better assessed using dependent parameters. Fig. 4 displays, as an example, the variation of stress amplitude (σ_a) with the number of cycles (N_f) at a fixed strain amplitude (ε_a = 0.8%, i.e. the same cases of Fig. 3) for the studied cases. In this representation, it can be seen that the cyclic stress–strain response exhibits three distinct stages, i.e. an initial stage with sudden variations of stress amplitude, followed by a dominant stage, in some cases a saturated-like stage, characterised by smooth changes, and a final stage with a rapid decrease of stress amplitude up to the total failure.

The variation of strain energy density with the number of cycles to failure at a fixed strain amplitude (ε_a = 0.8%, i.e. the same cases of Figs. 3 and 4) is shown in Fig. 5. The strain energy density is defined here as the sum of both the plastic and positive elastic components [39]. As shown, the more intense changes appear in the first cycles, as in the previous case. After that, the strain energy density varies smoothly until the final fracture. Despite the strain amplitude is fixed for all cases presented in Fig. 4 and Fig. 5, it is notorious a clear variation of the number of cycles to failure for the different tested steels.

3.2. Stable stress–strain response

Based on the conclusions drawn in the previous section, and as usual for high-strength steels, the stable stress–strain response was characterised using the half-life cycles (see Fig. 3). The half-life cycles obtained in the experiments for all tested materials are displayed in Fig. 6. It is clear from the figure that the shapes of the hysteresis loops are not only material dependent but also strain path dependent.

The cyclic stress–strain curve is an important tool to describe the stable material response. Fatigue design methods often require the knowledge of such curves to correlate the applied strain with the corresponding stress level [18,20,35]. The cyclic stress–strain curve can be written as follows:

$$\frac{\Delta\varepsilon}{2} = \frac{\Delta\sigma}{2E} + \left(\frac{\Delta\sigma}{2K'}\right)^{1/n'} \quad (1)$$

where K' is the cyclic strain hardening coefficient, and n' is the cyclic strain hardening exponent. This curve can be drawn by connecting the tensile and compressive tips of the stable stress–strain loops collected at different strain amplitudes. As shown in Fig. 6, the tips of the stable hysteresis loops are very close to the fitted curves, either for the ascending or the descending branches. Thus, we can conclude that the Ramberg-Osgood model satisfactorily describes the shapes of the stabilised hysteresis loops. The fitted constants for these materials, obtained via the least square method, are compiled in Table 3.

From an engineering point of view, the fatigue resistance can be defined using stress, strain, and energy parameters. Under strain-controlled conditions, the two last are generally more attractive. Regarding the strain-life relationship, a convenient approach to correlate these two variables is through the Coffin-Manson-Basquin (CMB) model, which accounts for both the elastic and plastic strain components:

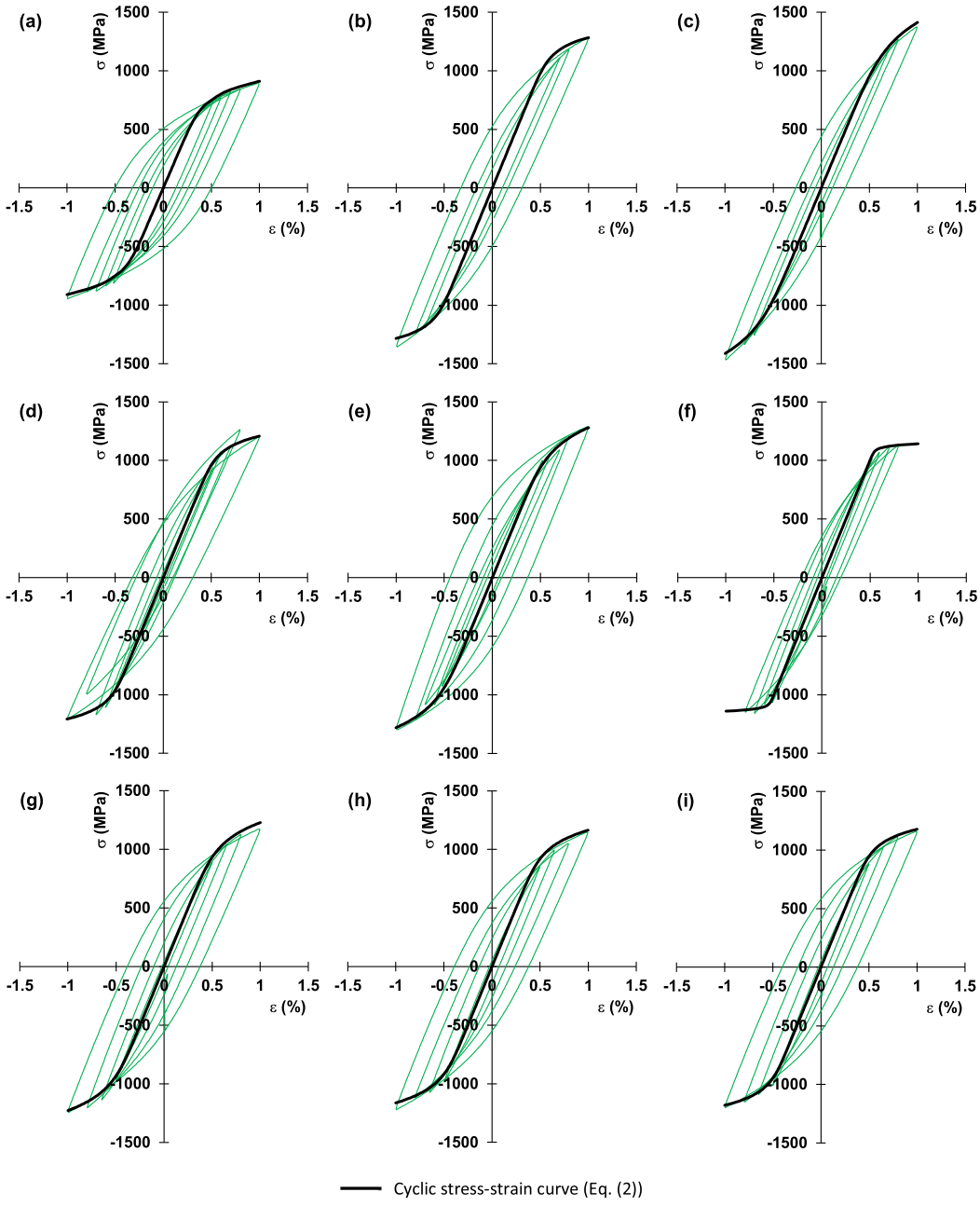

Fig. 6. Stable loops and cyclic stress–strain curves: (a) Steel 1; (b) Steel 2; (c) Steel 3; (d) Steel 4; (e) Steel 5; (f) Steel 6; (g) Steel 7; (h) Steel 8; (i) Steel 9.

Table 3
Constants of the cyclic stress–strain curves.

Material	Cyclic strain hardening coefficient, K' (MPa)	Cyclic strain hardening exponent, n'
Steel 1	1684	0.1172
Steel 2	1931	0.0722
Steel 3	3085	0.1330
Steel 4	1827	0.0748
Steel 5	2588	0.1251
Steel 6	1243	0.0158
Steel 7	2301	0.1129
Steel 8	2020	0.1008
Steel 9	1827	0.0798

$$\frac{\Delta\varepsilon}{2}=\frac{\Delta\varepsilon_e}{2}+\frac{\Delta\varepsilon_p}{2}=\frac{\sigma_f'}{E}(2N_f)^b+\varepsilon_f'(2N_f)^c \quad (2)$$

where $\Delta\varepsilon$ is the total strain range, $\Delta\varepsilon_e$ is the elastic strain range, $\Delta\varepsilon_p$ is the plastic strain range, σ_f' is the fatigue strength coefficient, E is the Young's modulus, b is the fatigue strength exponent, ε_f' is the fatigue ductility coefficient, and c is the fatigue ductility exponent. Fig. 7 shows the fitted functions for the different steels as well as the experimental data collected from the half-life cycles. As can be seen in the figure, each steel exhibits a distinct behaviour and the differences tend to increase for higher strain amplitudes. The values of the unknowns, determined using the least square method, are listed in Table 4.

Energy-life relationships are also very popular in fatigue design. Two of the most widespread energy-based approaches are the Smith-Watson-Topper (SWT) and the Liu models. Both models can also be established using the above-mentioned fatigue strength and the fatigue ductility

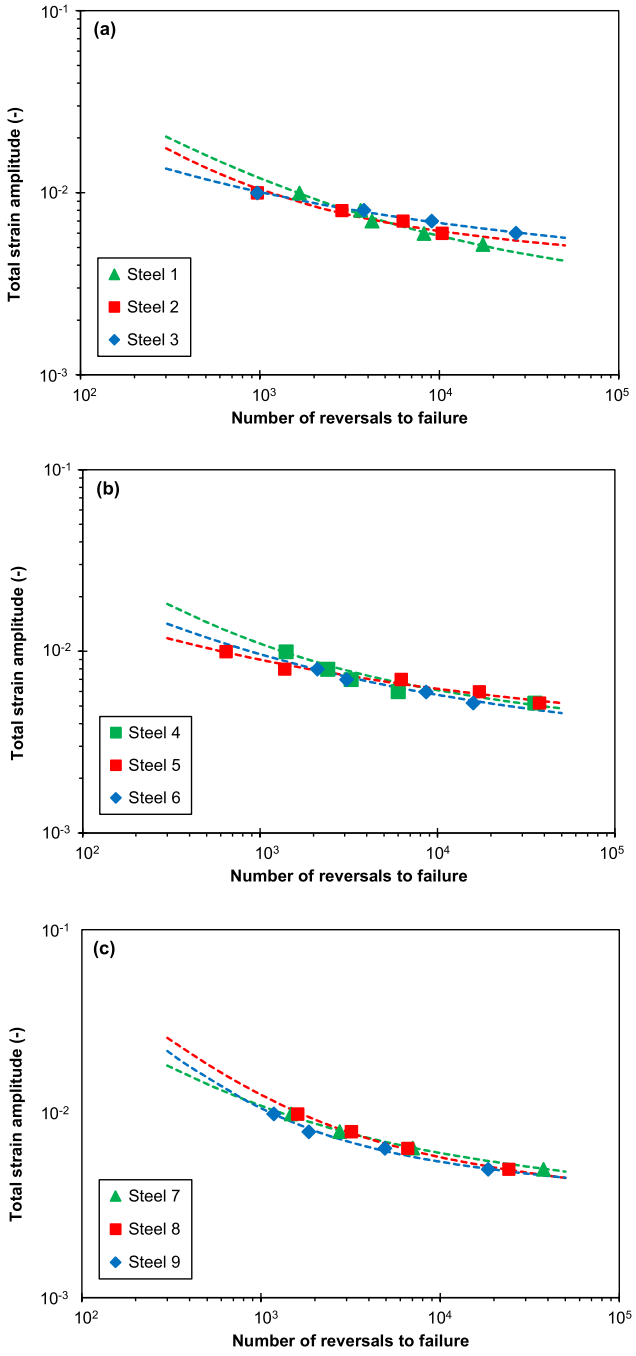

Fig. 7. Total strain amplitude versus number of reversals to failure: (a) bainitic steels (Steels 1 to 3); (b) martensitic steels (Steels 4 to 6); (c) low-carbon steels (Steels 7 to 9).

properties (see Table 4) and can be written by the following formulae, respectively:

$$\sigma_{max}\frac{\Delta\varepsilon}{2}=\frac{\sigma_f^{'2}}{E}(2N_f)^{2b}+\sigma_f^{'}\varepsilon_f^{'}(2N_f)^{b+c} \quad (3)$$

and

$$\Delta W=\Delta\sigma\,\Delta\varepsilon=\frac{4\,\sigma_f^{'2}}{E}(2N_f)^{2b}+4\,\sigma_f^{'}\,\varepsilon_f^{'}(2N_f)^{b+c} \quad (4)$$

where σ_{max} is the maximum stress, and $\Delta\sigma$ is the stress range. The former model is based on both the maximum tensile stress and the strain amplitude applied on the critical plane, while the latter is related to the virtual strain energy density applied in the component.

Table 4
Constants of the strain-life curves.

Material	Fatigue strength coefficient, $\sigma_f^{'}$ (MPa)	Fatigue strength exponent, b	Fatigue ductility coefficient, $\varepsilon_f^{'}$	Fatigue ductility exponent, c
Steel 1	1560	−0.0722	0.4876	−0.6080
Steel 2	2109	−0.0689	1.1015	−0.8168
Steel 3	2372	−0.0738	0.1370	−0.5535
Steel 4	2240	−0.0831	0.6927	−0.7223
Steel 5	1980	−0.0674	0.0881	−0.5014
Steel 6	1716	−0.0688	0.1970	−0.5535
Steel 7	2240	−0.0829	0.6927	−0.7227
Steel 8	2260	−0.0901	2.8636	−0.8793
Steel 9	2060	−0.0795	4.0091	−0.9764

Although energy-life approaches are often used in fatigue design, the most popular approaches are based on a single hysteresis loop, generally collected at the half-life, which is assumed to be representative of the saturated cyclic stress–strain response. The use of the cumulative strain energy density, as a fatigue indentifier parameter, despite it is not new, is much less frequent, as already discussed above [27–30]. Nevertheless, this parameter, which is related to the total energy absorbed to fracture, has led to good results, either under uniaxial loading or multiaxial loading [31–35]. The cumulative strain energy density (W_T) defined in accordance with the Ellyin's concept [38], i.e. by the sum of both the positive elastic and the plastic components, can be formalised as follows:

$$W_T=\sum_{i=1}^{N_f}\left(\Delta W_e^{+}+\Delta W_p\right)_i=\sum_{i=1}^{N_f}\Delta W_{T,i} \quad (5)$$

where ΔW_e^{+} is the positive elastic strain energy of the i^{th} hysteresis loop, ΔW_p is the plastic strain energy density of the i^{th} hysteresis loop, and N_f is the number of cycles to failure.

The variation of the cumulative strain energy density for the tested steels is presented in Fig. 8. As can be seen in the figure, this parameter is quite stable for the different tested steels and is almost independent of the Mn content for the bainitic steels (Fig. 8a) and also almost independent of the tempering temperature for the martensitic steels (Fig. 8b) and low-carbon steels (Fig. 8c). It is also evident that the cumulative strain energy density is a decreasing function of the strain amplitude. The relationship between W_T and $2N_f$ can be successfully fitted via power functions, i.e. straight lines on log–log scales:

$$W_T=\kappa\,(2N_f)^{\alpha} \quad (6)$$

where K and α are two material constants obtained from the experimental results. The unknowns computed in this case are compiled in Table 5. The dashed lines displayed in Fig. 8 were obtained for all points of each family (Steels 1 to 3 in the case of Fig. 8(a)); Steels 4 to 6 in the case of Fig. 8(b), and Steels 7 to 9 in the case of Fig. 8(c)) and can be interpreted as average functions. Overall, the average functions are quite close to the data points, which allows to correlate the cumulative strain energy density with the fatigue life for a given family using a very limited number of variables. The fitted constants for the average functions are listed in Table 6.

It is also interesting to note that the positive elastic strain energy density at the half-life cycle correlates closely with the cumulative strain energy density. As shown in Fig. 9, the dialectical relationship between these two variables can be established via power functions, i.e.

$$W_T=\kappa_e\left(\Delta W_{e,HL}^{+}\right)^{\alpha_e} \quad (7)$$

where $\Delta W_{e,HL}^{+}$ is the positive elastice strain energy density at the half-life cycle, and K_e and α_e are material constants obtained by using a best-fitting technique. The material constants computed for the different

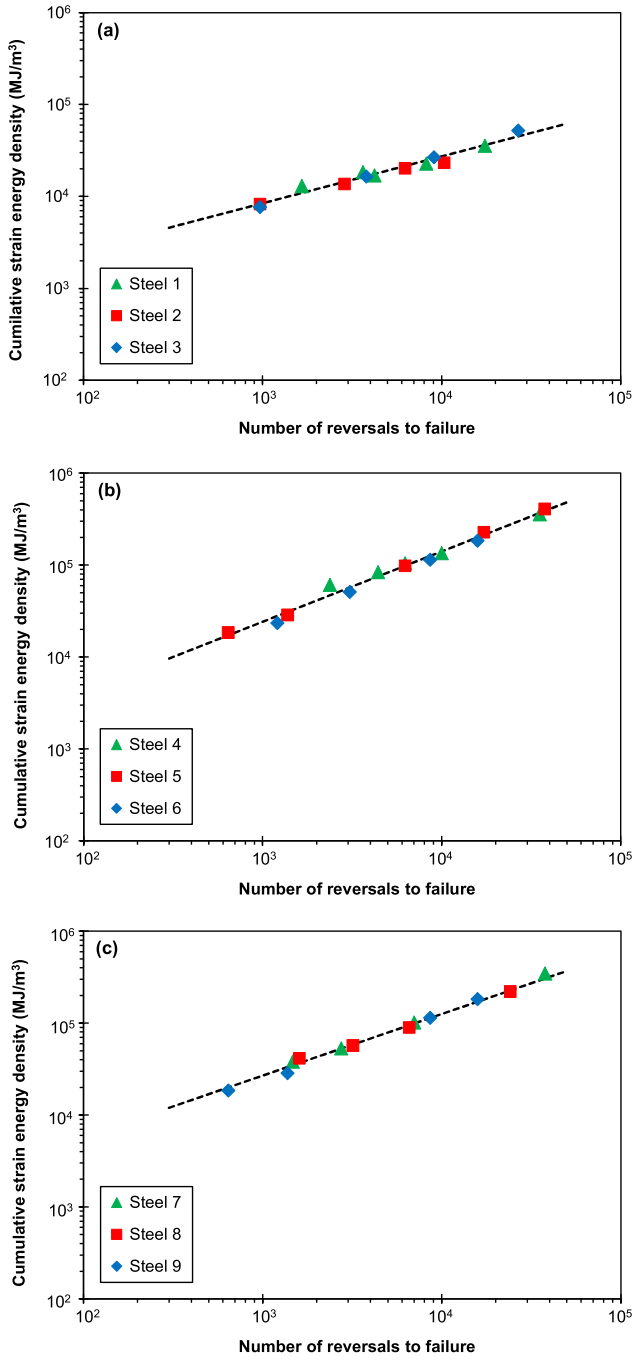

Fig. 8. Cumulative strain energy density versus number of reversals to failure: (a) bainitic steels (Steels 1 to 3); (b) martensitic steels (Steels 4 to 6); (c) low-carbon steels (Steels 7 to 9).

materials are exhibited in Table 7. In fact, Martins et al. [32] have already reported a power relationship between the cumulative strain energy density and the elastic strain energy density for rail steels subjected to uniaxial strain-controlled loading. For cyclic loading with $\sigma_{min} \leq 0$ ($R \leq 0$), the positive elastic strain energy density can be related to the maximum applied stress by:

Table 5
Constants of the cumulative energy-life curves.

Material	Coefficient α (MJ/m^3)	Exponent K
Steel 1	567.21	0.4176
Steel 2	383.24	0.4485
Steel 3	145.92	0.5746
Steel 4	343.46	0.6575
Steel 5	112.81	0.7774
Steel 6	81.90	0.7989
Steel 7	239.95	0.6876
Steel 8	395.01	0.6229
Steel 9	161.95	0.7251

Table 6
Constants of the cumulative energy-life curves by steel family.

Material	Coefficient α (MJ/m^3)	Exponent K
Bainitic steels	249.05	0.5096
Martensitic steels	122.60	0.7651
Low-carbon steels	261.71	0.6704

$$\Delta W^{+}_{e,HL} = \frac{\sigma^2_{max}}{2E} \quad (8)$$

where σ_{max} is the maximum applied stress at the half-life. This relationship is particularly useful because it allows a simple correlation between the maximum applied stress (which can be rapidly estimated from the cyclic curve) and the associated cumulative strain energy density.

3.3. Fatigue life predictions

In this study, the fatigue life predictions were carried out for all steels using five different models:

(1) Coffin-Manson (CM) model (see Eq. (2));
(2) Smith-Watson-Topper (SWT) model (see Eq. (3));
(3) Liu model (see Eq. (4));
(4) Cumulative strain energy density (W_T) model (see Eq. (6));
(5) Cumulative strain energy density model ($W_{T,a}$) using average W_T versus $2N_f$ functions.

In the case of the model based on the cumulative strain energy density, i.e. the Model 4, the maximum applied stress (see Eq. (8)) was estimated from the cyclic curve (Eq. (1)) allowing the calculation of $\Delta W^{+}_{e,HL}$ and, consequently, the value of the cumulative strain energy density (W_T) through Eq. (7). Then, Eq. (6) was used to estimate the number of reversals to failure ($2N_f$). Regarding the Model 5, the approach was similar to the previous one, but Eq. (6) was solved using the average W_T versus $2N_f$ functions (dashed lines of Fig. 8). As far as the SWT and the Liu models are concerned, the maximum stress (σ_{max}) and the stress range ($\Delta\sigma$) of Eq. (3) and Eq. (4), respectively, were computed using the cyclic curve (see Eq. (2)). Concerning the CM model, since it is based on the total strain amplitude, no previous calculations were needed.

Fig. 10 plots the experimental lives ($2N_{f,e}$) against the predicted lives ($2N_{f,p}$) obtained with the five above-mentioned models. Overall, all models led to good predictions, which is an interesting finding. The CM model is more accurate in this kind of analysis because the fatigue identifier parameter is defined directly from the strain amplitude, which is the controlled loading variable. We can also note that the SWT and the Liu models exhibit very similar predictions, which can be explained by the fact that under fully-reversed conditions, there is a direct

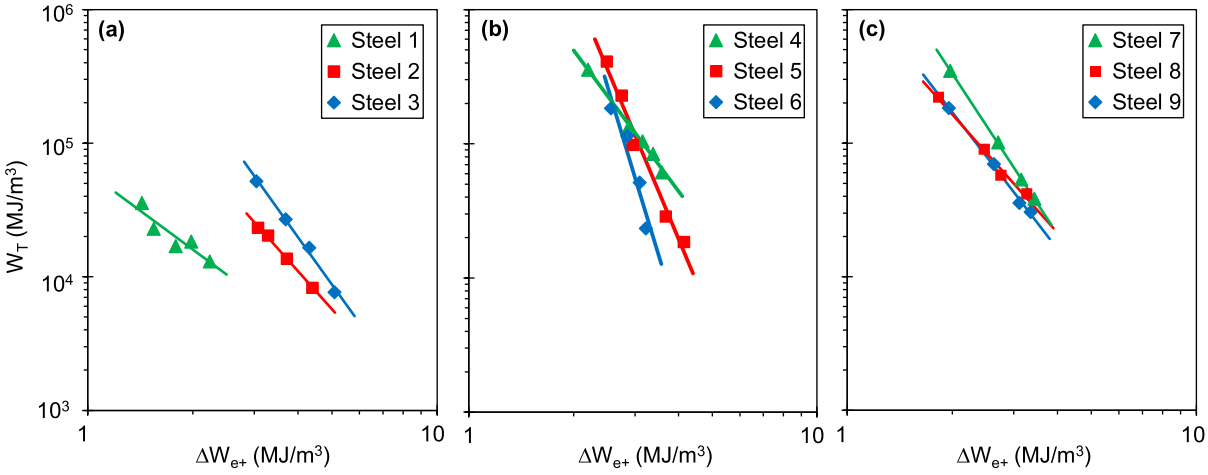

Fig. 9. Positive elastic strain energy density at the half-life (ΔW_{e+}) versus cumulative strain energy density (W_T) for the tested steels: (a) bainitic steels (Steels 1 to 3); (b) martensitic steels (Steels 4 to 6); (c) low-carbon steels (Steels 7 to 9).

Table 7
Constants of the W_T versus ΔW_e^+ curves.

Material	Coefficient α_e (MJ/m^3)	Exponent κ_e
Steel 1	60.62×10^3	−1.927
Steel 2	650.8×10^3	−2.944
Steel 3	3.123×10^6	−3.654
Steel 4	5.584×10^6	−3.491
Steel 5	1.050×10^6	−6.197
Steel 6	6.659×10^6	−8.539
Steel 7	5.211×10^6	−3.982
Steel 8	1.259×10^6	−2.940
Steel 9	1.781×10^6	−3.394

proportionality between both fatigue identifier parameters. Regarding the two models based on the cumulative strain energy density, the degree of accuracy is also quite similar.

In order to better compare the predictive capabilities of the tested models, a statisitical analysis based on the probability density function of the fatigue error was performed. The probability density function can be defined as follows:

$$Z(x) = \frac{1}{\delta\sqrt{2\pi}} e^{-(x-\mu)^2/(2\delta^2)} \tag{9}$$

where δ is the standard deviation, and μ is the mean value. The fatigue error (E_N) was calculated via the following equation:

$$E_N = \log_{10}\left(\frac{2N_{f,e}}{2N_{f,p}}\right) \tag{10}$$

where $2N_{f,w}$ is the experimental fatigue life, and $2N_{f,p}$ is the predicted fatigue life.

Fig. 11 shows the probability density functions of the fatigue errors for the different models considered in this study. Generally speaking, more accurate models are associated with mean values close to zero and lower standard deviations. As expected, the CM model exhibits the lower mean error and the lower standard deviation. Moreover, the SWT and the Liu models led to very similar probability density functions. Finally, the functions of the two models based on the cumulative strain energy density are slightly moved to the conservative side, which is interesting in the context of fatigue design. Moreover both models present slightly higher values of standard deviation. However, the results are acceptable, demonstrating that they are valid alternatives to the classical models.

It should also be noted that the model based on the average functions ($W_{T,a}$) is quite similar to that obtained from the individual fitting, which is a clear advantage since the cumulative strain energy density is almost independent of the Mn content or the tempering temperature, allowing a significant reduction of the number of low-cycle fatigue tests required to characterise the cyclic elastic–plastic behaviour of these families of advanced high-strength steels. In contrast, the other models (CM, SWT, or Liu) require individual fitting, which can be laborious, time-consuming, and expensive. In sum, the cumulative strain energy density is adequate to correlate the fatigue damage with the number of cycles to failure in advanced high-strength steels subjected to strain-control mode.

4. Conclusions

This paper addressed the use of the cumulative strain energy density as a fatigue indicator parameter in advanced high-strength steels subjected to uniaxial cyclic loading. Nine different steels, selected from three multiphase families, encompassing different chemical compositions and different heat treatment routes, were tested under strain-controlled conditions. The capabilities of the proposed model based on the cumulative strain energy density were compared with those of other classical models (namely the Coffin-Manson, Smith-Watson-Topper, and Liu models). The following conclusions can be drawn:

- The cyclic stress–strain response of these alloys comprised three distinct stages: a first stage with rapid variations of stress amplitude and strain energy density, followed by a dominant stable stage, and a short final stage of intense changes up to the total failure;
- The cumulative strain energy density versus the number of reversals to failure, unlike the classical strength-life and ductility-life relationships, was not particularly affected by the chemical composition or the heat treatment routes;

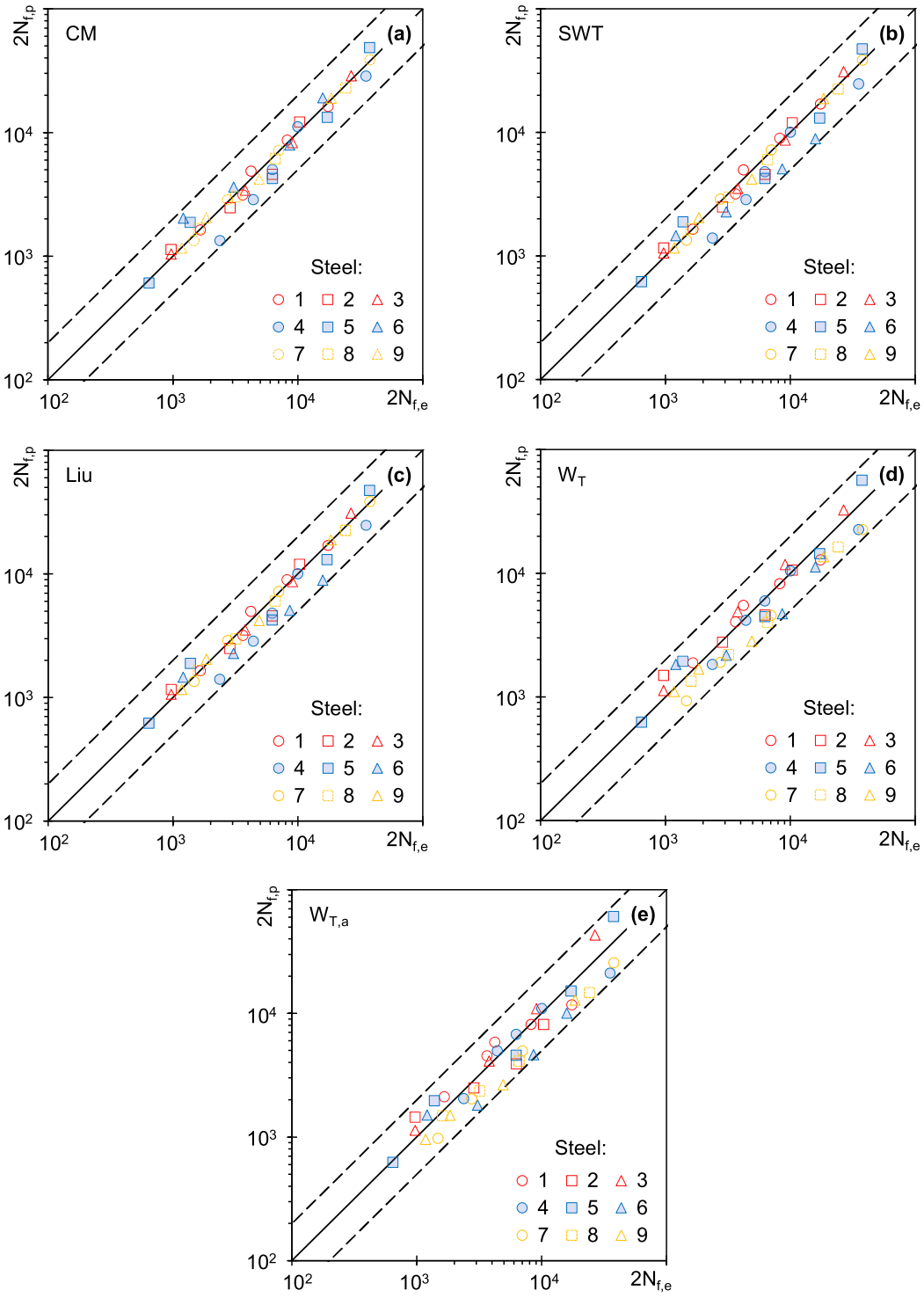

Fig. 10. Fatigue life predictions obtained with the different tested models: (a) CM; (b) SWT; (c) Liu; (d) W_T; (e) $W_{T,a}$.

- The models based on the cumulative strain energy density (individual fitting or average functions) led to good fatigue life predictions, marginally worse than the other studied approaches, but slightly more conservative;
- The model based on the average functions ($W_{T,a}$) exhibited almost similar predictive capabilities than the W_T model, which can be advantageous to reduce the time and cost associated with cyclic elastic–plastic characterisation of advanced high-strength steels.

Declaration of Competing Interest

The authors declare that they have no known competing financial interests or personal relationships that could have appeared to influence the work reported in this paper.

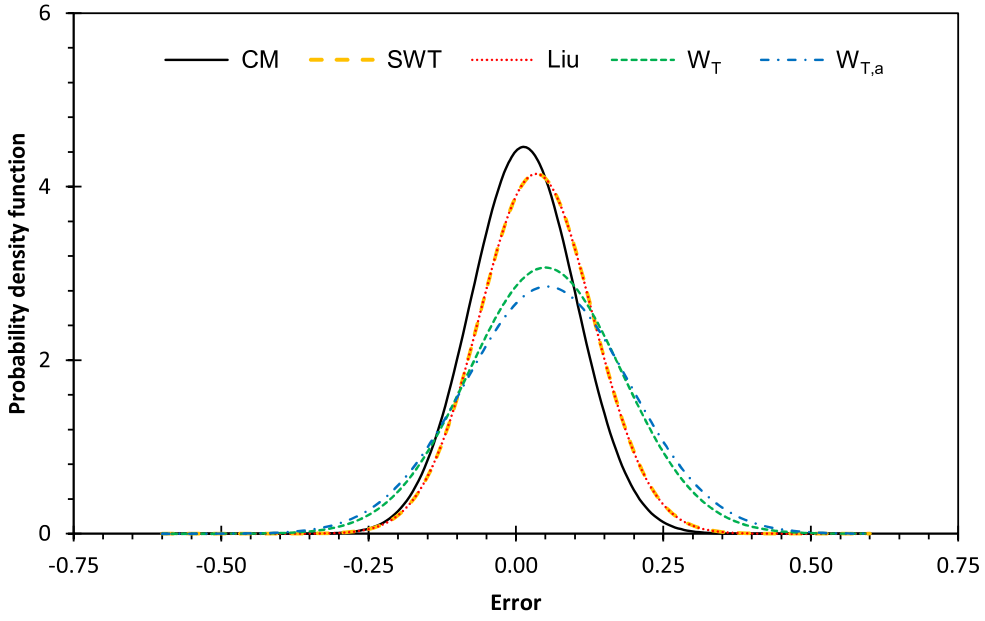

Fig. 11. Probability density functions of the fatigue error for the different tested models.

Acknowledgement

This research is sponsored by FEDER funds through the program COMPETE – Programa Operacional Factores de Competitividade – and by national funds through FCT – Fundação para a Ciência e a Tecnologia – under the projects UIDB/00285/2020 and UIDB/00667/2020.

References

[1] Gao GH, Zhang H, Tan ZL, Liu WB, Bai BZ. A carbide-free bainite/martensite/austenite triplex steel with enhanced mechanical properties treated by a novel quenching-partitioning-tempering process. Mater Sci Eng A 2013;559:165–9.
[2] Wang X, Liu C, Qin Y, Li Y, Yang Z, Long X, et al. Effect of tempering temperature on microstructure and mechanical properties of nanostructured bainitic steel. Mater Sci Eng A 2022;832:142357.
[3] Gao G, Zhang H, Tan Z, Liu W, Bai B. A carbide-free bainite/martensite/austenite triplex steel with enhanced mechanical properties treated by a novel quenching–partitioning–tempering process. Mater Sci Eng A 2013;559:165–9.
[4] Qin Y, Li X, Lv B, Long X, Yang Z, Zhang FC, et al. Effect of refined cementite on the microstructure and properties of nanostructured bainitic bearing steel. Mater Sci Eng A 2022;797:140220.
[5] Long XY, Zhang FC, Zhang CY. Effect of Mn content on low-cycle fatigue behaviors of low-carbon bainitic steel. Mater Sci Eng A 2017;697:111–8.
[6] Taddesse AT, Zhu S-P, Liao D, Keshtegar B. Cyclic plastic zone-based notch analysis and damage evolution model for fatigue life prediction of metals. Mater Des 2022;191:108639.
[7] Susmel L. Notches, nominal stresses, fatigue strength reduction factors and constant/variable amplitude multiaxial fatigue loading. Int J Fat 2022;162:106941. https://doi.org/10.1016/j.ijfatigue.2022.106941.
[8] Cruces AS, Mokhtarishirazabad M, Moreno B, Zanganeh M, Lopez-Crespo P. Study of the biaxial fatigue behaviour and overloads on S355 low carbon steel. Int J Fat 2020;143:105466.
[9] Nejad RM, Liu Z. Effect of periodic overloads and spectrum loading on fatigue life and microstructure in a Grade 900A rail steel. Theor Appl Fract Mech 2020;110:102796.
[10] Deng QY, Zhu SP, He JC, Li XK, Carpinteri A. Multiaxial fatigue under variable amplitude loadings: Review and solutions. International Journal of Structural Integrity 2022;13(3):349–93.
[11] Zhu S-P, Lei Q, Huang H-Z, Yang Y-J, Peng W. Mean stress effect correction in strain energy-based fatigue life prediction of metals. Int J Damage Mech 2017;26:1219–41.
[12] Correia JAFO, Raposo P, Muniz-Calvente M, Blasón S, Lesiuk G, De Jesus AMP, et al. A generalization of the fatigue Kohout-Věchet model for several fatigue damage parameters. Eng Fract Mech 2017;185:284–300.
[13] Pejkowski Ł, Seyda J. Fatigue of four metallic materials under asynchronous loadings: Small cracks observation and fatigue life prediction. Int J Fat 2021;142:105904.
[14] Marciniak Z, Rozumek D, Macha E. Fatigue lives of 18G2A and 10HNAP steels under variable amplitude and random non-proportional bending with torsion loading. Int J Fat 2008;30:800–13.
[15] Zhu S-P, Liu Y, Liu Q, Yu Z-Y. Strain energy gradient-based LCF life prediction of turbine discs using critical distance concept. Int J Fat 2018;113:33–42.
[16] Carpinteri A, Berto F, Campagnolo A, Fortese G, Ronchei C, Scorza D, et al. Fatigue assessment of notched specimens by means of a critical plane-based criterion and energy concepts. Theor Appl Fract Mech 2016;84:57–63.
[17] Rozumek D, Marciniak Z, Lachowicz CT. The energy approach in the calculation of fatigue lives under non-proportional bending with torsion. Int J Fat 2010;32:1343–50.
[18] Lesiuk G, Szata M, Rozumek D, Marciniak Z, Correia J, Jesus A. Energy response of S355 and 41Cr4 steel during fatigue crack growth process. J Strain Anal Eng Des 2018;53:663–75.
[19] Macek W, Łagoda T, Mucha N. Energy-based fatigue failure characteristics of materials under random bending loading in elastic-plastic range. Fatigue Fract Eng Mater Struct 2018;41:249–59.
[20] Liao D, Zhu S-P. Energy field intensity approach for notch fatigue analysis. Int J Fat 2019;127:190–202.
[21] Zhou G, Kuang J, Song W, Qian G, Berto F. Fatigue failure transition evaluation of load carrying cruciform welded joints by effective notch energy model. Eng Fail Anal 2022;138:106328.
[22] Yang S, Sun J. Multiaxial fatigue life assessment of 304 austenitic stainless steel with a novel energy-based criterion. Int J Fat 2022;159:106728.
[23] Benedetti M, Berto F, Le Bone L, Santus C. A novel Strain-Energy-Density based fatigue criterion accounting for mean stress and plasticity effects on the medium-to-high-cycle uniaxial fatigue strength of plain and notched components. Int J Fat 2020;133:105397.
[24] Berto F, Lazzarin P, Yates JR. Multiaxial fatigue of V-notched steel specimens: a non-conventional application of the local energy method. Fatigue Fract Eng Mater Struct 2011;34(11):921–43.
[25] Branco R, Costa JD, Prates PA, Berto F, Pereira C, Mateus A. Load sequence effects and cyclic deformation behaviour of 7075–T651 aluminium alloy. Int J Fat 2022;155:106593.
[26] Colin J, Fatemi A. Variable amplitude cyclic deformation and fatigue behaviour of stainless steel 304L including step, periodic, and random loadings. Fatigue Fract Eng Mater Struct 2010;33(4):205–20.
[27] Halford GR. The energy required for fatigue (Plastic strain hysteresis energy required for fatigue in ferrous and nonferrous metals). J Mater 1966;1:3–18.
[28] Li DM, Nam WJ, Leea CS. Strain energy–based approach to the low-cycle fatigue damage mechanism in a high-strength spring steel. Metall Mater Trans A 1998;29:1431–9.
[29] Long XY, Branco R, Zhang FC, Berto F, Martins RF. Influence of Mn addition on cyclic deformation behaviour of bainitic rail steels. Int J Fat 2020;132:105362.
[30] Ho HS, Zhou WL, Li Y, Liu KK, Zhang E. Low-cycle fatigue behavior of austenitic stainless steels with gradient structured surface layer. Int J Fat 2020;134:105481.
[31] Shi G, Gao Y, Wang X, Cui Y. Energy-based low cycle fatigue analysis of low yield point steels. J Constr Steel Res 2018;150:346–53.
[32] Martins RF, Branco R, Long XL. Fatigue life assessment in bainitic steels based on the cumulative strain energy density. Appl Sci 2020;10:7774.
[33] Sarkar PP, De PS, Dhua SK, Chakraborti PC. Strain energy based low cycle fatigue damage analysis in a plain C-Mn rail steel. Mater Sci Eng A 2017;707:125–35.
[34] Callaghan MD, Humphries SR, Law M, Ho M, Bendeich P, Li H, et al. Energy-based approach for the evaluation of low cycle fatigue behaviour of 2.25Cr–1Mo steel at elevated temperature. Mater Sci Eng A 2010;527:5619–23.

[35] Branco R, Prates P, Costa JD, Cruces A, Lopez-Crespo P, Berto F. On the applicability of the cumulative strain energy density for notch fatigue analysis under multiaxial loading. Theor Appl Fract Mech 2022;120:103405.
[36] Yang G, Xia SL, Zhang FC, Branco R, Long XY, Li YG, et al. Effect of tempering temperature on monotonic and low-cycle fatigue properties of a new low-carbon martensitic steel. Mater Sci Eng A 2021;826:141939.
[37] Xia S, Zhang FC, Yang Z. Microstructure and mechanical properties of 18Mn3Si2CrMo steel subjected to austempering at different temperatures below Ms. Mater Sci Eng A 2018;724:103–11.
[38] Plumtree A, Abdel-Raouf HA. Cyclic stress-strain response and substructure. Int J Fatigue 2001;23:799–805.
[39] Ellyin F. Fatigue Damage, Crack Growth and Life Prediction, 1st ed.; Chapman & Hall: London, UK, ISBN 0-412-59600-8; 1997.